Cross-Process Interference in Single-Cycle Electron Emission from Metal Needle Tips

Anne Herzig,[1] Peter Hommelhoff,[2] Eleftherios Goulielmakis,[1] Thomas Fennel,[1,*] and Lennart Seiffert[1,†]
[1]Institute of Physics, University of Rostock, D-18059 Rostock, Germany
[2]Faculty of Physics, Ludwig Maximilian University Munich, D-80799 Munich, Germany
and Department of Physics, Friedrich Alexander University Erlangen-Nuremberg, D-91058 Erlangen, Germany

(Received 8 August 2025; revised 7 November 2025; accepted 17 December 2025; published 12 February 2026)

Though interference from different emission channels enabled a deeper understanding of strong-field photoemission in atoms and molecules, it remained out of reach for solids. Here, we explore metal needle tips under single-cycle pulses via classical trajectories extended by quantum interference and numerical solution of the time-dependent Schrödinger equation. We find interference of direct and backscattered electrons with fringe pattern encoding subcycle information on birth times and near-field driven acceleration dynamics, opening routes for ultrafast solid-state metrology.

DOI: 10.1103/n482-q85k

Strong-field ionization spotlights classical and quantum properties of photoemission in at least three ways [1–5]. First, classical trajectories of direct and backscattered electrons predict the cutoff features at $2U_p$ and $10U_p$, respectively [6–9] [see Fig. 1(a)], where U_p denotes the ponderomotive energy. Second, corresponding quantum trajectories explain above-threshold ionization (ATI) with photoelectron peaks separated by the photon energy of the laser field [Fig. 1(a)]. The energy separation $\Delta E_{el} = \Delta(\hbar\omega_{el}) = \hbar\omega$ emerges from intercycle interference of wave packets emitted in subsequent laser field cycles with period $T = 2\pi/\omega$ according to $\Delta\omega_{el}T = 2\pi$, resembling a temporal double-slit [10,11] [see Fig. 1(b)]. Third, additional spectral modulations on a larger energy scale (orange curve) can be attributed to intracycle interference of trajectories originating from a single half-cycle [cf. Fig. 1(b)] [12,13], highlighting the rich physical information encoded in the spectra.

Intra- and intercycle interferences typically arise from different quantum pathways of the same processes, e.g., direct or backscattered electrons. However, cross-process interference [CPI, cf. Fig. 1(b)] between pathways of different processes can also yield characteristic spectral features. For atomic and molecular targets, these include holographic signatures from interference between direct and revisiting electrons [14–16] encoding, e.g., Coulomb focusing and minute deflection due to interaction with the residual ion. The visibility of CPI crucially depends on quenching competing interference effects using intense single-cycle optical waveforms, which confine electron emission to one cycle. The availability of such fields enabled unprecedented attosecond metrologies for atoms [17], nanostructures [18], and solids [19]. Whereas interferences from revisiting and backscattered electrons were observed for molecules [15], the physics of CPI of direct and backscattered electrons is not understood.

Here we show that such CPI can be exposed by also suppressing revisiting electrons by using needle tips. To explore the underlying physics, we consider needle tip photoemission under carrier-envelope phase (CEP) controlled single-cycle pulses [cf. Fig. 2(a)]. Our quantum simulations based on the solution of the time-dependent Schrödinger equation (TDSE) for a simplified model system predict strongly CEP-dependent photoelectron spectra

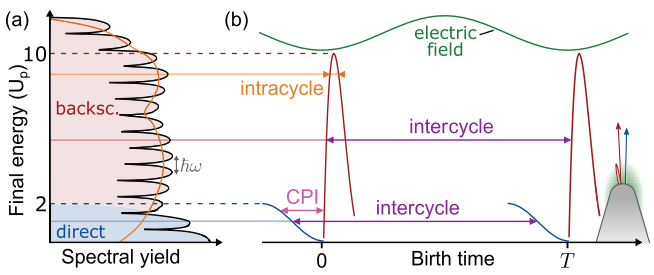


FIG. 1. Interference mechanisms in strong-field photoemission. (a) Schematic sketch of an energy spectrum with typical cutoffs at $2U_p$ for direct electrons (blue shaded) and $10U_p$ for backscattered electrons (red shaded), ATI peaks, and additional modulation due to intracycle interference (orange). (b) Illustration of birth time-dependent final energies (blue: direct, red: backscattered). Arrows and lines indicate constructive interference: intercycle (purple), intracycle (orange), and possible cross-process (magenta) interference.

*Contact author: thomas.fennel@uni-rostock.de
†Contact author: lennart.seiffert@uni-rostock.de

Published by the American Physical Society under the terms of the Creative Commons Attribution 4.0 International license. Further distribution of this work must maintain attribution to the author(s) and the published article's title, journal citation, and DOI.

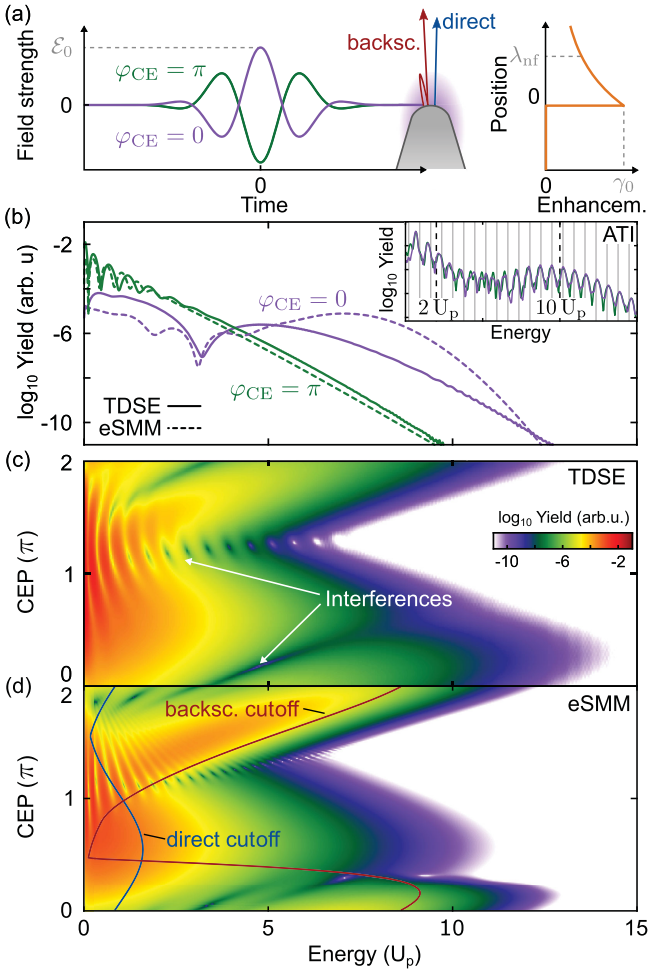


FIG. 2. CPI in single-cycle driven strong-field electron emission from a metal needle tip. (a) Purple and green curves show the incident pulses for two different CEPs (as indicated). Blue and red curves visualize electrons emitted directly and after elastic backscattering. The orange curve shows the spatially decaying near-field profile. (b) Energy spectra extracted from TDSE (solid) and eSMM (dashed) simulations for the two CEPs as in (a). The inset shows TDSE spectra for long pulses (12 cycles) and expected ATI peak positions (gray lines). (c,d) CEP-dependent energy spectra from TDSE and eSMM simulations. Blue and red curves in (d) indicate the CEP-dependent cutoff energies for direct emission and backscattering.

containing distinct interference features. Comparison with an extended trajectory model verifies that these features originate from CPI of direct and backscattered electrons and encode information on their relative spectral phase, which is of key importance for the temporal and spectral characterization of the ultrashort emitted wave packets [18].

The intrinsic restriction of free electronic motion to only one half-space for needle tips automatically limits emission to half-cycles with electric field vectors pointing into the tip and ensures that returning electrons can escape only after backscattering. Despite this seemingly limiting feature and additional modifications due to inhomogeneous near-fields [20,21], field propagation [22], or charge interactions [23,24], strong-field photoemission from needle tips (and nanospheres) resembles the atomic picture to a large extent [25–27]. For example, application of the (quantum) trajectory picture to needle tip photoemission uncovered the duration of subcycle tunneling [28] and revealed the generation of the shortest electronic signal to date using single-cycle light fields [18].

The employed quantum description is adapted from Ref. [29] and reflects the common one-dimensional approximation of nanotip photoemission along the tip's symmetry axis [2,4,28]. In brief, we solve the one-dimensional TDSE for a single active electron in the spatiotemporal potential $V(x,t) = V_0(x) + V_{nf}(x,t)$, where the box potential $V_0(x)$ models a metallic tip with work function W. The time-dependent potential $V_{nf}(x,t) = e\int_0^x E_{nf}(x',t)\mathrm{d}x'$ reflects the near-field $E_{nf}(x,t) = \gamma(x)E_{las}(t)$ resulting from the single-cycle waveform $E_{las}(t)$ [purple and green curve in Fig. 2(a)] and the spatial field enhancement profile

$$\gamma(x) = \begin{cases} 1 + (\gamma_0 - 1)\exp(-x/\lambda_{nf}) & x \geq 0 \\ 0 & x < 0 \end{cases}, \quad (1)$$

with peak near-field enhancement $\gamma_0 = 7$ and decay length $\lambda_{nf} = 100$ Å as for a typical tungsten tip [20,24,26] [orange curve in Fig. 2(a)]. We note that a power-law description as in Ref. [20] or varying the decay length does not modify our results significantly (see Sec. II of Supplemental Material [30]). We describe single-cycle waveforms $E_{las}(t) = -[\partial/\partial t]\mathcal{A}(t)$ via the vector potential

$$\mathcal{A}(t) = \frac{\mathcal{E}_0}{\omega}\cos(\omega[t - t_0] + \varphi_{\mathcal{A}})\exp\left(-\frac{(t-t_0)^2}{2\tau^2}\right) \quad (2)$$

with peak field strength $\mathcal{E}_0$, central angular frequency ω, duration τ, and the phase $\varphi_{\mathcal{A}} = \varphi_{CE} + \pi/2$, where φ_{CE} is the CEP. This ensures $\int_{-\infty}^{\infty} E_{las}(t')\mathrm{d}t' = 0$. We consider single-cycle pulses with 800 nm central wavelength, peak intensity 1×10^{12} W/cm^2, and a duration of $\tau_{FWHM} = 2\sqrt{\ln 2}\tau = \pi/\omega \approx 1.3$ fs (intensity FWHM). The resulting peak intensity at the tip surface of 4.9×10^{13} W/cm^2 corresponds to a ponderomotive potential of $U_p = 2.98$ eV.

The photoelectron spectra predicted by the TDSE in Figs. 2(b) and 2(c) exhibit three main features. First, the spectra are strongly CEP dependent and do not show clear cutoffs around $2U_p$ and $10U_p$ for direct emission and backscattering [1] as predicted for long pulses [cf. inset in Fig. 2(b)]. Second, they exhibit unevenly spaced fringe features with a strongly CEP-dependent structure and contrast. Third, around $\varphi_{CE} = 0$ no discernible fringes but a pronounced dip can be found.

To explore the origin of these features we performed a semiclassical trajectory analysis [6–9] extended by quantum interference and effective spectral broadening.

Trajectories launched at rest for birth times t_0 at the classical tunneling exit $x_{te} = -W/E_{nf}(0, t_0)$ are propagated classically in the local near-field according to

$$\ddot{x}(t) = -\frac{e}{m_e} E_{nf}[x(t), t]. \tag{3}$$

For trajectories returning to the surface ($x = 0$) we assume elastic backscattering ($\dot{x} \to -\dot{x}$). Each trajectory yields a final energy $E_f(t_0)$ and momentum $p_f(t_0)$ and contributes to the spectrum with a weight $\Gamma(t_0)$ determined from the WKB tunneling rate. This "simple man's model" (SMM) predicts CEP-dependent cutoff energies for direct and backscattered electrons [cf. blue and red curves in Fig. 2(d)] that reveal a phase-dependent switching of the dominant emission process: for $\varphi_{CE} \approx 0.7\pi$ direct electrons reach higher energies than rescattered ones. This represents a remarkable difference to few-cycle or two-color excitation, where the cutoff modulation typically reflects only backscattered electrons [26–29]. However, the conventional SMM yields unrealistically sharp spectral cutoff features [29] and fully neglects interference effects.

To account for quantum interference and effective spectral broadening [26,31], we describe each trajectory via the energy-dependent complex amplitude

$$\psi(E, t_0) = A(E, t_0) e^{i\theta(E)}. \tag{4}$$

Here $A(E, t_0)$ describes spectral broadening according to a Gaussian wave packet in momentum space, expressed in terms of energy via

$$A(E, t_0) = c\sqrt{\Gamma(t_0)} e^{-\frac{(\sqrt{E_f(t_0)} - \sqrt{E})^2}{\sigma^2}}, \tag{5}$$

with normalization constant c and spectral width σ^2. The effective phase function $\theta(E)$ in Eq. (4) is constructed in WKB approximation from the set of birth times for which trajectories match the considered energy E via phase-correct accumulation of respective amplitudes according to

$$\theta(E) = \arg\left\{ \int_{-\infty}^{t} \sqrt{\Gamma(t_0)}\, e^{\frac{i}{\hbar} S_c(t_0, t)} \delta[E - E_f(t_0)] \mathrm{d}t_0 \right\}. \tag{6}$$

In the compensated action

$$S_c(t_0, t) = S(t_0, t) - p_f(t_0) x(t) + E_f(t_0) t \tag{7}$$

the trivial time dependence associated with the asymptotic drift motion is removed such that the effective phase becomes stationary for sufficiently late evaluation time t. The trajectory-specific classical action required to evaluate the effective phase reads [32]

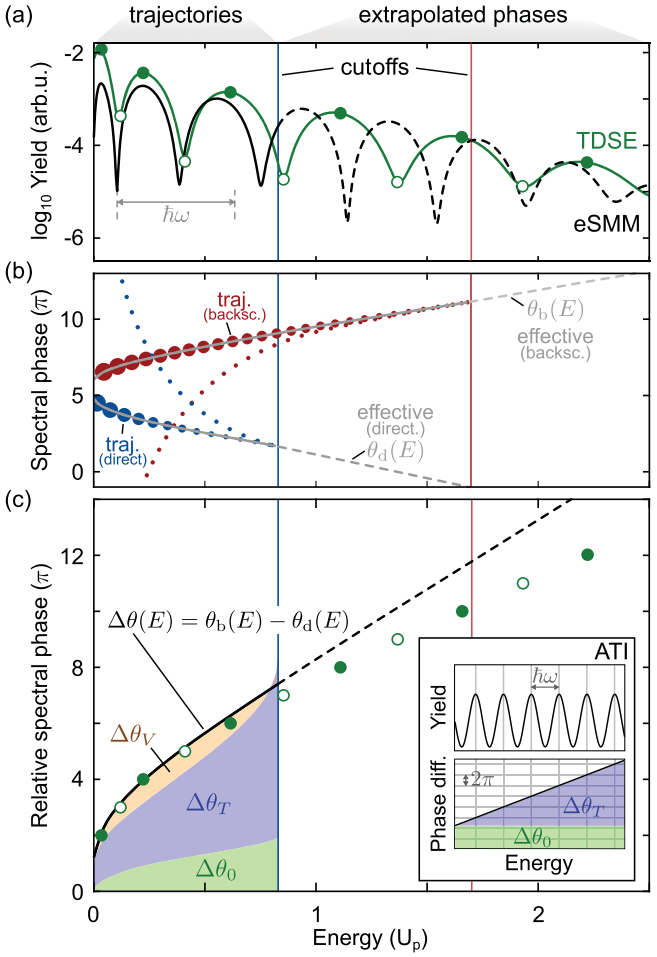


FIG. 3. Fringe-spacing of CPI and relative spectral phase contributions. (a) Energy spectra calculated with eSMM (black) and TDSE (green) for $\varphi_{CE} = 1.1\pi$. The dashed part indicates the eSMM-spectrum beyond the classical cutoff (cf. vertical blue and red lines for direct and backscattered trajectories) where phases are extrapolated. (b) Blue and red symbols show final phases and energies of individual direct and backscattered trajectories. The size illustrates the trajectories' weights (see Sec. I of Supplemental Material [30] for details). Curves indicate the final energy-dependent effective phases for the two trajectory classes, which are extrapolated linearly beyond the respective cutoff energies (dashed). (c) Relative spectral phases $\Delta\theta$ between backscattered and direct electrons extracted from the eSMM simulations (black curve) and from the minima and maxima of the TDSE spectrum in (a) (open and closed green symbols). Shaded areas visualize individual contributions of the eSMM trajectories from the birth time $\Delta\theta_0$ (light green), the kinetic energy $\Delta\theta_T$ (blue), and the (near-field) potential $\Delta\theta_V$ (orange). Note that we included the phase compensation resulting from Eq. (7) in the kinetic energy contribution. The inset shows a respective representation for ATI.

$$S(t_0, t) = \underbrace{W t_0}_{\hbar\theta_0} + \underbrace{\int_{t_0}^{t} \frac{m_e}{2} v^2(t') \mathrm{d}t'}_{\hbar\theta_T} \underbrace{- \int_{t_0}^{t} V_{nf}(x(t'), t') \mathrm{d}t'}_{\hbar\theta_V}. \tag{8}$$

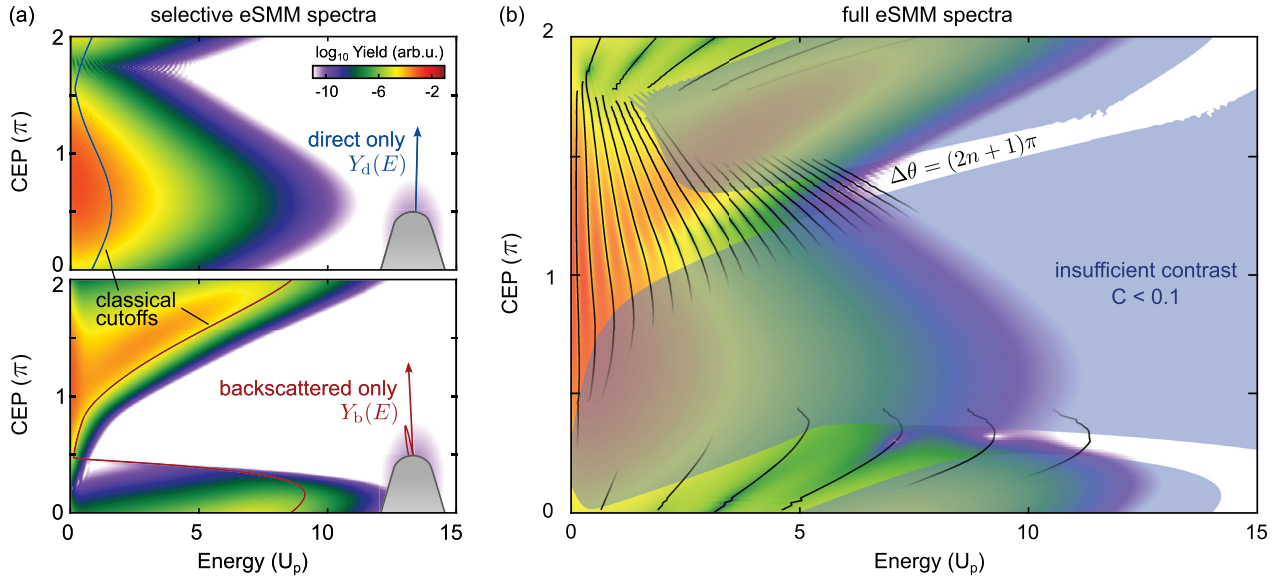


FIG. 4. Requirements for the emergence of CPI. (a) CEP-dependent selective eSMM spectra $Y_d(E)$ and $Y_b(E)$ for direct and backscattered electrons (as indicated). Curves indicate the classical cutoffs as in Fig. 2(d). (b) CEP-dependent full eSMM spectra [as in Fig. 2(d)] showing CPI when two conditions are fulfilled: (1) high CPI contrast, $C(E) > 0.1$, indicated by the nonshaded area, and (2) sufficiently fast energy evolution of the relative spectral phase $\Delta\theta(E)$. Black curves indicate odd multiples of π, resulting in destructive interference.

The three phase contributions encode birth time (θ_0), kinetic energy evolution (θ_T), and phase accumulation within a potential (θ_V)—in our case the near-field potential. We emphasize that the latter contribution is neglected within the commonly employed strong-field approximation, but is crucial to capture the near-field effect in our scenario. Although the near-field implicitly enters the kinetic energy contribution via the velocity, explicit consideration of the potential term is crucial to capture the phase evolution. Note that a trajectory-selective analysis of the phase can yield multiple contributions for a given energy [cf. symbols in Fig. 3(b)] while the effective phase is dominated by the trajectories with particularly high weight (see Supplemental Material [30] for details). Selective application of the above procedure to direct and backscattered electrons yields the corresponding effective phase functions $\theta_d(E)$ and $\theta_b(E)$ up to the specific cutoff energies (solid curves) and are linearly extrapolated beyond (dashed curves). Note that an additional phase shift of π is included upon backscattering.

Within this "extended simple man's model" (eSMM), energy spectra follow from integration of the process-selective complex amplitudes $\psi_d(E, t_0)$ and $\psi_b(E, t_0)$ over all birth times via

$$Y(E) = \left| \int [\psi_d(E, t_0) + \psi_b(E, t_0)] \mathrm{d}t_0 \right|^2. \tag{9}$$

Best agreement with the TDSE results is found for $\sigma_d^2 = 1.97$ eV and $\sigma_b^2 = 0.36$ eV in the spectral broadening. Though our approximation is not strictly norm conserving, which would require an advanced description by, e.g., wave packet molecular dynamics [33], we find remarkable agreement with TDSE [compare Figs. 2(b) and 2(d) to Figs. 2(b) and 2(c)]. Discrepancies around $\varphi_{CE} \approx 1.4\pi$ or 0.5π are attributed to less accurate phase extrapolation due to vanishing cutoffs of direct or backscattered electrons. However, the CEP-dependent spectral modulation as well as the pronounced interference structures are reproduced, supporting that eSMM captures the central physics and is suited for its further detailed analysis.

Regarding the pronounced interference features, the eSMM unambiguously reveals that the fringes result from CPI of direct and backscattered electrons, because the interference vanishes in the individual spectra [cf. $Y_d(E)$ and $Y_b(E)$ in Fig. 4(a)]. Only minor residual intercycle interference remains in signals from direct ($\varphi_{CE} \approx 1.8\pi$) and backscattered ($\varphi_{CE} \approx 0.2\pi$) electrons. The selective spectra further explain that the CPI contrast

$$C(E) = \frac{2\sqrt{Y_d(E)}\sqrt{Y_b(E)}}{Y_d(E) + Y_b(E)} \tag{10}$$

is responsible for the emergence of CPI fringes only in specific spectral regions as highlighted via a contrast mask in Fig. 4(b). An additional prerequisite is a rapidly changing relative spectral phase $\Delta\theta(E) = \theta_b(E) - \theta_d(E)$ of direct and backscattered electrons. In this case, constructive and destructive interference [cf. black curves in Fig. 4(b)] alternate with energy, leading to fringes. Hence,

CPI only becomes visible in regions with sufficiently high contrast and rapidly evolving relative spectral phase.

Having identified the prerequisites for CPI fringes, we now explore the physics encoded in their particular shape, namely their energy-dependent position and spacing. The representative example in Fig. 3(a) shows that the spacing does not match the photon energy (gray arrow) and that the eSMM prediction evolves very similarly to the TDSE result up to the classical cutoff of direct electrons (compare solid black to green curve). The larger deviation at higher energies is attributed to the uncertainties resulting from the required phase extrapolation. These results remain robust when varying the relevant parameters (see Sec. II of Supplemental Material [30]). The relative spectral phase evolution from eSMM [black curve in Fig. 3(c)] can further be decomposed into the individual contributions from birth time, kinetic energy, and (near-field) potential (shaded areas). For comparison, we also extract the relative spectral phase evolution from the minima and maxima in the TDSE spectrum [open and closed green symbols in Figs. 3(a) and 3(c)].

Three central conclusions can be drawn from this comparison. First, the eSMM result matches the evolution of the TDSE result remarkably well up to the direct electron cutoff and also the extrapolation shows the same trend, i.e., a linear evolution with energy beyond the cutoff, albeit with a slightly different slope. Second, focusing on the region below the cutoff shows that the slope of the relative spectral phase decreases with energy, explaining the increasing spacing of the fringes. Third and most importantly, it is imperative to take all three relative spectral phase contributions into account, in particular the contribution of the potential, which is commonly completely neglected. This is in fundamental contrast to the case of ATI in longer pulses, where this contribution perfectly cancels for trajectories from adjacent cycles and the strictly linear evolution of the kinetic energy term with energy creates equally spaced peaks, separated by the photon energy [see inset in Fig. 3(c)]. The fact that all three contributions (birth time, kinetic energy, and potential) enter the relative spectral phase evolution in a nontrivial way opens routes for their selective investigation via the CPI fringe structure.

In conclusion, our theoretical analysis of single-cycle driven photoemission from sharp needle tips predicts robust CEP-dependent interference structures by cross-process interference of direct and backscattered electrons. Comparison of TDSE results with an extended simple man's model reveals under which conditions CPI occurs and how the nontrivial fringe pattern can be explained with the relative spectral phase evolution of direct and backscattered electrons. Our findings highlight that CPI fringes encode a distinct contribution from the near-field potential that extends beyond the established quantum trajectory description within strong-field approximation. The CPI features from direct and backscattered electrons contain rich information on the near-field-driven acceleration dynamics and provide a sensitive fingerprint for the amplitude and phase of the corresponding wave packets. This feature promises both a new metrology concept for the characterization of ultrashort electron pulses and deeper insights into the boundary between classical and pure quantum physics of strong-field-induced subcycle electron dynamics. Their robustness with respect to laser and near-field parameters suggest that experimental realization for nanotips, nanoparticles, or lithographically produced nanometer-sharp structures is likely feasible with current technology. Our Letter provides a first step toward a theoretical toolbox to analyze such phenomena and to develop corresponding reconstruction approaches in the future.

Acknowledgments—We thank Philip Dienstbier for fruitful discussions. We acknowledge financial support from the German Research Foundation (DFG) via CRC 1477 "Light-Matter Interactions at Interfaces" (ID: 441234705).

Data availability—The data that support the findings of this article are openly available [34].

[1] F. Krausz and M. Ivanov, Rev. Mod. Phys. **81**, 163 (2009).
[2] P. Dombi, Z. Pápa, J. Vogelsang, S. V. Yalunin, M. Sivis, G. Herink, S. Schäfer, P. Groß, C. Ropers, and C. Lienau, Rev. Mod. Phys. **92**, 025003 (2020).
[3] M. Krüger, M. Schenk, M. Förster, and P. Hommelhoff, J. Phys. B **45**, 074006 (2012).
[4] M. Krüger, C. Lemell, G. Wachter, J. Burgdörfer, and P. Hommelhoff, J. Phys. B **51**, 172001 (2018).
[5] L. Seiffert, S. Zherebtsov, M. F. Kling, and T. Fennel, Adv. Phys. X **7**, 2010595 (2022).
[6] P. B. Corkum, Phys. Rev. Lett. **71**, 1994 (1993).
[7] J. L. Krause, K. J. Schafer, and K. C. Kulander, Phys. Rev. Lett. **68**, 3535 (1992).
[8] K. J. Schafer, B. Yang, L. F. DiMauro, and K. C. Kulander, Phys. Rev. Lett. **70**, 1599 (1993).
[9] G. G. Paulus, W. Becker, W. Nicklich, and H. Walther, J. Phys. B **27**, L703 (1994).
[10] F. Lindner, M. G. Schätzel, H. Walther, A. Baltuška, E. Goulielmakis, F. Krausz, D. B. Milošević, D. Bauer, W. Becker, and G. G. Paulus, Phys. Rev. Lett. **95**, 040401 (2005).
[11] D. G. Arbó, E. Persson, and J. Burgdörfer, Phys. Rev. A **74**, 063407 (2006).
[12] D. G. Arbó, K. L. Ishikawa, K. Schiessl, E. Persson, and J. Burgdörfer, Phys. Rev. A **81**, 021403 (2010).
[13] N. I. Shvetsov-Shilovski and M. Lein, Phys. Rev. A **97**, 013411 (2018).
[14] R. Gopal, K. Simeonidis, R. Moshammer, T. Ergler, M. Dürr, M. Kurka, K.-U. Kühnel, S. Tschuch, C.-D. Schröter, D. Bauer, J. Ullrich, A. Rudenko, O. Herrwerth, T. Uphues, M. Schultze, E. Goulielmakis, M. Uiberacker, M. Lezius, and M. F. Kling, Phys. Rev. Lett. **103**, 053001 (2009).
[15] T. Khurelbaatar, J. Heo, S. Yu, X. Lai, X. Liu, and D. E. Kim, Light Sci. Appl. **13**, 108 (2024).

[16] Y. Huismans *et al.*, Science **331**, 61 (2011).
[17] M. T. Hassan, T. T. Luu, A. Moulet, O. Raskazovskaya, P. Zhokhov, M. Garg, N. Karpowicz, A. M. Zheltikov, V. Pervak, F. Krausz, and E. Goulielmakis, Nature (London) **530**, 66 (2016).
[18] H. Y. Kim, M. Garg, S. Mandal, L. Seiffert, T. Fennel, and E. Goulielmakis, Nature (London) **613**, 662 (2023).
[19] A. Moulet, J. B. Bertrand, T. Klostermann, A. Guggenmos, N. Karpowicz, and E. Goulielmakis, Science **357**, 1134 (2017).
[20] G. Herink, D. R. Solli, M. Gulde, and C. Ropers, Nature (London) **483**, 190 (2012).
[21] J. Heimerl, S. Meier, A. Herzig, F. L. Hoffmann, L. Seiffert, D. Lesko, S. Hillmann, S. Wittigschlager, T. Weitz, T. Fennel, and P. Hommelhoff, Nat. Phys. **21**, 1893 (2025).
[22] F. Süßmann, L. Seiffert, S. Zherebtsov, V. Mondes, J. Stierle, M. Arbeiter, J. Plenge, P. Rupp, C. Peltz, A. Kessel, S. A. Trushin, B. Ahn, D. Kim, C. Graf, E. Rühl, M. F. Kling, and T. Fennel, Nat. Commun. **6**, 7944 (2015).
[23] L. Seiffert, P. Henning, P. Rupp, S. Zherebtsov, P. Hommelhoff, M. F. Kling, and T. Fennel, J. Mod. Opt. **64**, 1096 (2017).
[24] J. Schötz, L. Seiffert, A. Maliakkal, J. Blöchl, D. Zimin, P. Rosenberger, B. Bergues, P. Hommelhoff, F. Krausz, T. Fennel, and M. F. Kling, Nanophotonics **10**, 3769 (2021).
[25] S. Zherebtsov, T. Fennel, J. Plenge, E. Antonsson, I. Znakovskaya, A. Wirth, O. Herrwerth, F. Süßmann, C. Peltz, I. Ahmad, S. A. Trushin, V. Pervak, S. Karsch, M. J. J. Vrakking, B. Langer, C. Graf, M. I. Stockman, F. Krausz, E. Rühl, and M. F. Kling, Nat. Phys. **7**, 656 (2011).
[26] M. Krüger, M. Schenk, and P. Hommelhoff, Nature (London) **475**, 78 (2011).
[27] B. Piglosiewicz, S. Schmidt, D. J. Park, J. Vogelsang, P. Groß, C. Manzoni, P. Farinello, G. Cerullo, and C. Lienau, Nat. Photonics **8**, 37 (2014).
[28] P. Dienstbier, L. Seiffert, T. Paschen, A. Liehl, A. Leitenstorfer, T. Fennel, and P. Hommelhoff, Nature (London) **616**, 702 (2023).
[29] L. Seiffert, T. Paschen, P. Hommelhoff, and T. Fennel, J. Phys. B **51**, 134001 (2018).
[30] See Supplemental Material at http://link.aps.org/supplemental/10.1103/n482-q85k for more details on (1) the extraction of the effective phase and (2) the robustness of our models for different parameters, which includes Refs. [20,28,29].
[31] P. Dienstbier, Strong-field physics at nanoemitters in tailored complex light-fields, Ph.D. thesis, 2022.
[32] Y. Goldfarb, J. Schiff, and D. J. Tannor, J. Chem. Phys. **128**, 164114 (2008).
[33] P. E. Grabowski, *A Review of Wave Packet Molecular Dynamics* (Springer, Cham, 2014), pp. 265–282, 10.1007/978-3-319-04912-0_10.
[34] A. Herzig, P. Hommelhoff, E. Goulielmakis, T. Fennel, and L. Seiffert, Dataset for Manuscript "Cross-process interference in single-cycle electron emission from metal needle tips" (2025), 10.18453/rosdok_id00005037.